ASME Journal of Mechanisms and Robotics
Online journal at:
https://asmedigitalcollection.asme.org/mechanismsrobotics

Wenbo Jia
College of Mechanical and Electrical Engineering,
Nanjing University of Aeronautics
and Astronautics,
Nanjing 210016, China
e-mail: 052210820@nuaa.edu.cn

Teng Wang
College of Mechanical and Electrical Engineering,
Nanjing University of Aeronautics
and Astronautics,
Nanjing 210016, China

Baohua Zhao
College of Mechanical and Electrical Engineering,
Nanjing University of Aeronautics
and Astronautics,
Nanjing 210016, China

Wenzhuo Huang
College of Mechanical and Electrical Engineering,
Nanjing University of Aeronautics
and Astronautics,
Nanjing 210016, China

Yuzhou Duan
College of Mechanical and Electrical Engineering,
Nanjing University of Aeronautics
and Astronautics,
Nanjing 210016, China

Zuoqing Yu
College of Mechanical and Electrical Engineering,
Nanjing University of Aeronautics
and Astronautics,
Nanjing 210016, China

Jie Ling[1]
College of Mechanical and Electrical Engineering,
Nanjing University of Aeronautics
and Astronautics,
Nanjing 210016, China
e-mail: meejling@nuaa.edu.cn

Design of a Patient-Specific Needle Insertion Device for Accurate and Safe Lumbar Puncture

Robotic-assisted lumbar puncture (LP) has demonstrated significant advantages over manual procedures in terms of accuracy and repeatability, with robotic-assisted needle insertion devices (RNIDs) serving as the core component for accurate needle placement. However, current RNIDs still encounter critical limitations in needle tip deflection and complex construction. The patient-specific design, based on preoperative imaging and tissue mechanical properties, may potentially improve the aforementioned issues. This article proposes a one-degree-of-freedom (1-DOF) patient-specific RNID to enhance the insertion accuracy. The 1-DOF motion coupling both insertion and rotation is achieved through a replaceable helical-type inner liner bush (RHILB), which functions as the RNID's core transmission component. The RHILB features a patient-specific insertion-rotation ratio (IRR) determined from preoperative X-ray imaging. Utilizing three-dimensional (3D) printing technology, these customized RHILBs can be rapidly manufactured and seamlessly integrated into the RNID via a plug-and-play interface, enabling quick replacement for different patients. The preliminary experiments are conducted first to demonstrate the optimal IRRs for different materials. The kinematic model of the core component, i.e., the RHILB, is established. A fifth-order transition curve equation is formulated to eliminate impacts on velocity and acceleration during insertion. Prototype experiments are conducted to evaluate the insertion accuracy and patient-specific issues. Comparative results show that the variable-IRR design reduces mean needle tip deflection by 27.73% ($p < 0.05$) and 62.40% ($p < 0.001$) than the constant IRR design. [DOI: 10.1115/1.4069673]

Keywords: biomedical devices, mechanism synthesis and analysis, mechanisms and robots

1 Introduction

Lumbar puncture (LP) is a critical diagnostic and therapeutic procedure that uses a fine flexible needle to access the spinal canal [1]. This procedure requires millimeter accuracy in needle placement to precisely position the needle tip within the constrained epidural space (5–17 mm width) [2]. Conventional LP procedure employs a landmark-based blind insertion technique, where clinicians rely primarily on subjective tactile feedback from the needle base to assess the depth of insertion. This approach demonstrates limited tactile discrimination ability between different tissue layers [3,4]. Compared with manual operation, the advancements in robotic-assisted needle-based intervention evolve LP procedures mainly through a robotic-assisted needle insertion device (RNID), demonstrating three principal advantages in needle maneuverability, needle insertion accuracy, and repeatability [5–7].

Generally, RNIDs have two degrees-of-freedom (DOFs) in motion: a translational DOF for insertion and a rotational DOF

[1]Corresponding author.

Contributed by the Mechanisms and Robotics Committee of ASME for publication in the Journal of Mechanisms and Robotics. Manuscript received May 5, 2025; final manuscript received August 23, 2025; published online September 18, 2025. Assoc. Editor: James Yang.

for angular adjustment. Generally, the rotational DOF is arranged in series behind the translational DOF, with each DOF driven and controlled by a dedicated motor module [8,9]. The operational workflow of RNIDs generally involves three phases: (1) the preoperative phase that involves processing computed tomography (CT) images to construct a model of the target lesion and plan the insertion trajectory; (2) the needle adjustment phase that modifies the needle configuration according to the preoperative CT images; and (3) the needle insertion phase that performs automatic guidance for needle placement [8,9]. Ehrampoosh proposed an RNID for minimally invasive surgery, and its end effector drives a curved needle along a precomputed trajectory. During the insertion process, a proximal force sensor mounted on the robot measures the forces of needle–tissue interaction. When integrated with real-time data on rotational speed and position feedback, this information enables precise adaptive correction of the needle tip's actual position. Mechanical latch mechanisms ensure that the needle is securely locked in position at the beginning of the insertion cycle and is safely released upon completion [10]. In Lu's work, a probe with concentric electrodes collects signals first during puncture and converts them into spectral data. The main computer processes these data in real time to identify tissue types (e.g., skin, adipose, ligament, and cerebrospinal fluid). Based on this identification, a single DOF stepper motor drives the needle to achieve precise positioning within a translation distance of less than 2 mm [11]. In Xuan's work, a scanning path is first planned, acquired 2D spinal ultrasound images, and reconstructed into a three-dimensional (3D) model using optical tracker data. The transverse processes are first identified to locate the vertebrae, followed by the designation of puncture points by surgeons. Subsequently, the system calculates the kinematics of the robotic arm to align the needle with the planned trajectory, adjusts the puncture cannula for precise angular positioning, and inserts the needle through the cannula using a distal mechanism [12]. However, existing RNIDs face critical limitations: most rely on at least two motor modules for their two DOFs, resulting in bulky designs that hinder maneuverability, and they lack patient-specific customization for needle insertion, making generic RNIDs ill-suited for complex or atypical cases.

Despite the advantages of RNID, the needle is prone to bend during insertion, significantly reducing the accuracy of the puncture [13–15]. To address the issue of bending and deviation in the beveled needle, researchers have conducted extensive studies and innovations, such as optimizing puncture angles [16], developing more stable assistive devices or robots [17], and investigating puncture path planning and guidance techniques [8,18,19]. Other researchers, inspired by the parasitic wasp ovipositors, have developed self-propelling needles [20]. Compared with the direct push method, the self-propelling needle can effectively reduce tissue displacement and strain, thereby minimizing tissue damage during the needle insertion process [21]. This technique has been applied in multiple fields, such as prostate puncture [22]. However, this innovation was not explicitly used to reduce the tip deflection, and the mechanical structure was relatively complex. Recent studies have shown that rotational needle insertion can effectively reduce deviation and improve insertion accuracy [23–25]. According to the patterns and functions of rotation, it is classified into two subcategories: (1) intermittent rotation, namely, the rotation is intermittent during insertion to change the steering direction; and (2) duty-cycled rotation, namely, the rotation motion is periodic with duty cycles. For intermittent rotation, it will cause a large out-of-plane error when performing a unidirectional, large-angled rotation. To reduce the error, it is necessary to model the torsional dynamics and design a controller for error compensation [26]. For duty-cycled rotation, the trajectory of the insertion path is helical [27]. That can in real-time modify the steering path when inserted into tissue. However, existing studies have not fully explored the adaptability of rotational needle insertion in puncturing different tissue layers. This may lead to an increase in the needle deflection. Therefore, this article hypothesizes that there exists an optimal insertion-rotation ratio (IRR) for puncturing different tissue layers that minimize needle deflection.

In summary, current RNID technologies still exhibit the following limitations: (1) conventional RNIDs are usually driven by two motor modules, leading to a large form factor and poor maneuverability; (2) generic RNID lacks patient-specific customization for needle insertion, making it ill-suited for complex or atypical cases; (3) existing studies have not fully explored the influence of different IRRs on needle deflection when puncturing different tissue layers.

This study designs a series of experiments to investigate the adaptability of rotational needle insertion in puncturing different tissue layers with different biomechanical properties. The experiments find that each tissue layer has an optimal IRR value. This optimal IRR achieves the smallest deflection at the same insertion depth. Based on this finding, this study proposes a variable-IRR rotational needle insertion mechanism, which is designed for multilayer tissue puncture. This mechanism combines 3D printing technology. Through mechanical design, it can dynamically adjust the IRR parameter during insertion. This approach simplifies the DOFs of the drive mechanism and effectively improves the insertion accuracy for multilayer tissues.

To this end, this article proposes a 1-DOF RNID with a replaceable helical-type inner liner bush (RHILB), which is patient-specific to reduce needle deflection during insertion. Figure 1 shows the application of RNID (using the RHILB) in lumbar puncture surgeries. The RHILB is the key component that converts a simple motor rotation into the necessary insertion-rotation-coupled motion for the needle. The proposed RHILB is installed within the device to perform this critical motion conversion. Furthermore, the RHILB is designed to be replaceable, allowing IRR to be adjusted for different tissues. To realize the patient-specific purpose, the geometric parameters of the RHILB are determined by the specific CT data. Moreover, to eliminate rigid and soft impacts, a transition curve is used to optimize the RHILB. Lastly, the proposed RHILB is 3D printed and replaceable by a simple plug-and-play operation. The key contributions are as follows.

- Demonstrating that tissues with different mechanical properties correspond to different optimal IRRs.
- Designing an insertion-rotation-coupled 1-DOF RNID characterized by a RHILB. The RHILB is designed according to the patient-specific preoperative CT, easily fabricated by 3D printing, and rapidly replaced through a plug-and-play pattern.
- Introducing a transition curve model to RHILB, which could smoothly change the IRRs during insertion, avoiding rigid and soft impacts.

The remainder of this article is organized as follows. Section 2 focuses on validating the experimental theoretical basis and presenting key research hypotheses; Sec. 3 describes device design and working principle; Sec. 4 is a mathematical derivation of transition curves; Sec. 5 confirms that RHILB can increase puncture accuracy,

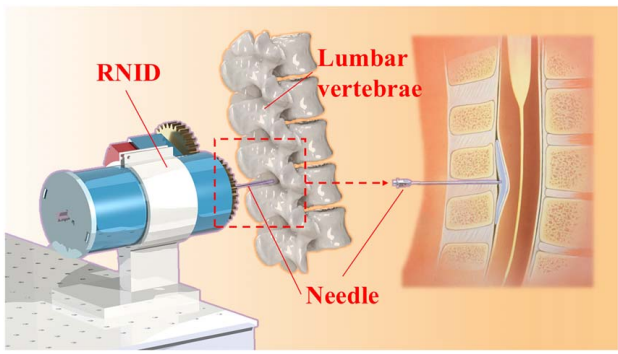

Fig. 1 Schematic diagram of the application of RNID (using RHILB) in the lumbar puncture surgery

and the actual motion curve of the needle is strongly correlated with the theoretical curve; Secs. 6 and 7 provide discussions and conclusions of limitations and potential future research directions.

2 Validation of Optimal Insertion and Rotation Ratio

In this section, preliminary experiments are performed to validate the hypothesis proposed in this article: there are different optimal IRRs for different kinds of tissues.

2.1 Experiment Setup and Parameters Determination. The experimental platform is shown in Fig. 2. Two independently controlled motors were used to generate the rotational and translational motions of a common RNID, allowing precise regulation of the IRR. The needle and force sensor were rigidly secured within the needle protector, which was connected to motor A via a coupling. Motor A itself was fixed on a lead screw-driven motion platform that was driven by motor B to achieve the transmission of motion. Two materials are selected as puncture targets: material A (LDX/V6, Blue Butterfly Medical Model Co., Ltd, China) with a similar mechanical property of the skin and material B (soft silicone, Guoyuan Technology Co., Ltd, China) with a similar mechanical property of adipose tissue. Taking material B as an example: during silicone preparation, we formulated it to standard softness with a Shore C hardness of approximately 5–10 C. Given that Young's modulus of human adipose tissue ranges between 5 and 50 kPa—equivalent to approximately 3–8 C on the Shore C scale—material B exhibits comparable mechanical properties to adipose tissue. Thus, we employed material B to simulate human adipose tissue in needle puncture experiments. Based on the same principle, material A is selected to simulate human skin.

When measuring the experimental results, we used an optical image measuring instrument (3D-family-VMS250, Greatest Idea Strategy Co., Ltd, China) to measure deflection.

To ensure coaxial alignment during the needle puncture procedure and positional precision of the insertion point, two fixtures were designed: a needle guide fixture for trajectory stabilization and an insertion template with designated needle entry ports. The fixtures and protector were made by 3D printing (Future P8200pro resin, WeNext Technology Co., Ltd, China). To measure insertion force, a flexible piezoresistive force sensor (SBT674, SIMBATOUCH Co., Ltd, China) was incorporated into the base of the needle. A sample test paper was placed at the end of the puncture material to capture the puncture exit point, allowing quantitative measurement of needle deflection.

2.2 Influence on Needle Deflection. During the experiments, the puncture depth is set at 40 mm for both materials. The preliminary IRR of materials A and B was set to a range of 2–40 mm/r (sampling interval: 2 mm/r), and a nonrotational control group was established.

The pulse transmitter (CL-01A Single-Axis Intelligent Controller, Beijing Haijiejiachuang Technology Co., Ltd, Beijing, China) was configured to achieve the desired IRR. For each ratio, an empty puncture (without material) and four material-filled punctures were performed, then we obtained the puncture result that one empty puncture point and four material-filled puncture points were performed on the sample test paper, as shown in Fig. 2(*a*). The data on the deflection distance were collected from the paper with an empty and four material-filled punctures. Upon completion of preliminary experiments and data, two optimal ranges of IRR were identified for materials A and B. Subsequently, a second refined experiment was performed with a sampling range of 10 mm/r and an interval of 0.5 mm/r, performing the same steps as in the previous experiment. This refinement process yielded experimental results with improved precision. The procedure was repeated for both materials in all ratios. The entire image of the working principle is illustrated in Fig. 2(*b*).

2.3 Results and Analysis. The puncture deflection for each experimental group was measured using an optical influence measurement instrument model VMS250. To improve the precision of the results, the largest outlier among the four deflection measurements in each group was discarded, and the remaining data were averaged to obtain the mean deflection value. The processed data from the first experiment were plotted as composite line graphs with IRR (mm/r) on the *x*-axis and the deflective distance (mm) on the *y*-axis, as shown in Figs. 3(*a*) and 3(*b*).

As illustrated in Figs. 3(*a*) and 3(*b*), the average puncture deflection for material A in the IRR range 10–20 mm/r was approximately 52% lower than that of nonrotational punctures, 12% lower than the range of 0–10 mm/r, 53% lower than the range of 20–30 mm/r, and 58% lower than the range of 30–40 mm/r. These results indicate that the optimal IRR for material A is within the 10–20 mm/r range. Similarly, material B exhibited an optimal IRR range of 20–30 mm/r. Based on these findings, a second refined experiment was conducted to achieve higher precision. Following the same methodology, data from the second experiment were processed and plotted as composite line graphs, as shown in Fig. 3(*c*) and 3(*d*). These results revealed that the minimal deflection for material A occurred at the IRR of 12 mm/r (deflection: 0.75 mm), while material B demonstrated its minimal deflection at the IRR of 26 mm/r (deflection: 0.50 mm).

Through the above experiments, it was determined that under identical puncture conditions and depth, material A exhibited an optimal IRR of 12 mm/r, while material B demonstrated an optimal IRR of 26 mm/r. These findings conclusively validate the

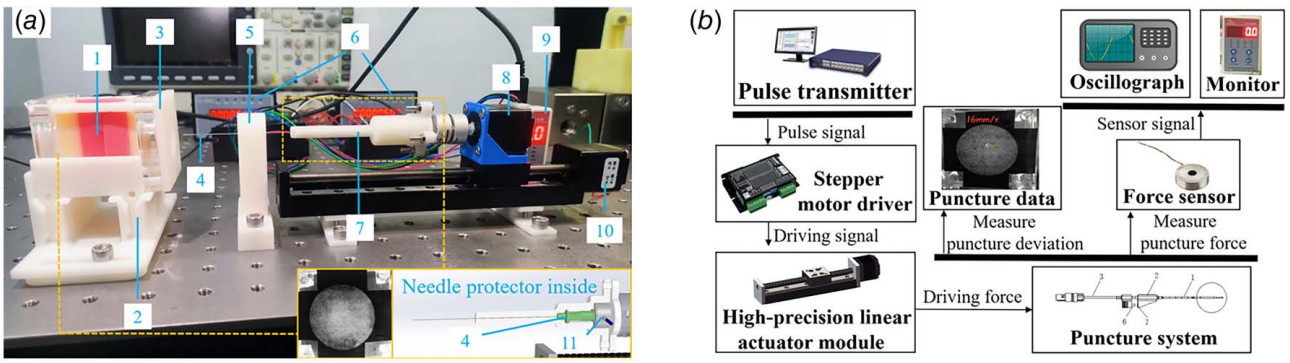

Fig. 2 Experimental setup and signal diagram. (*a*) Pre-experimental platform. Bottom right: section view of the needle protector. Middle: the sample of the test paper. (*b*) The working principle flowchart. (1) Puncture material, (2) material fixture, (3) insertion template, (4) needle, (5) needle guide fixture, (6) pulse transmitter, (7) needle protector, (8) motor A, (9) force signal display, (10) high-precision linear actuator module, and (11) force sensor.

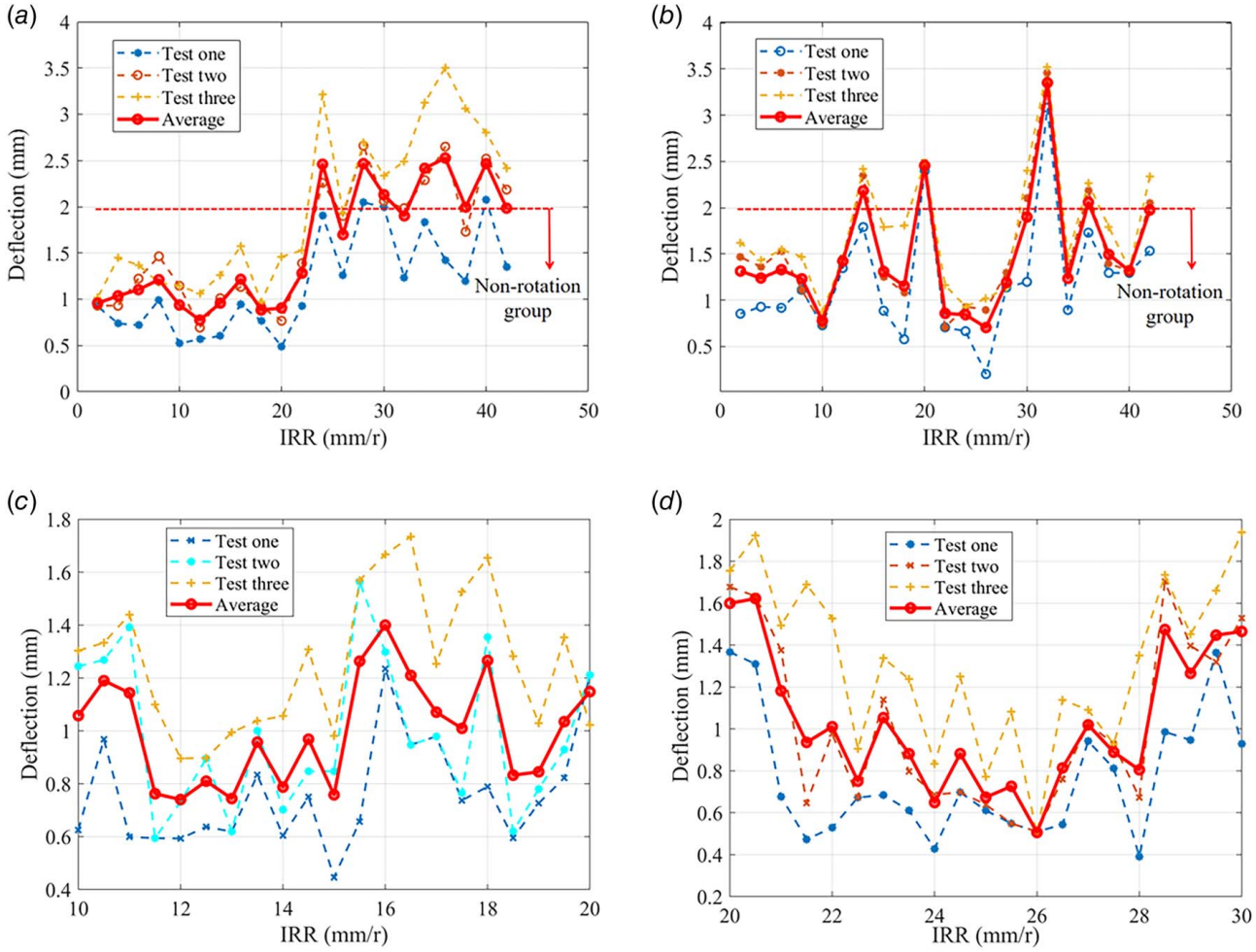

Fig. 3 The results of the experiments. (*a*) Material A chart of the relationship between deflection and IRR. Dotted line: the nonrotational group result. (*b*) Material B chart of the relationship between deflection and IRR. Dotted line: the nonrotational group result. (*c*) The refined experimental material A chart of the relationship between deflection and IRR. (*d*) The refined experimental material B chart of the relationship between deflection and IRR.

hypothesis that there are different optimal IRRs for different puncture materials.

3 Device Design and Working Principle

Our preliminary experiments have demonstrated that there are distinct optimal IRRs for different tissues. To adapt the IRR as the needle punctures each tissue layer, the RHILB was designed to drive the needle to finish the coupled motion of insertion and rotation. The pitches of RHILB vary continuously, and each pitch height is confirmed by the tissue thickness distribution obtained preoperatively, ensuring that the optimal IRR of the currently punctured tissue was applied to the tissue being punctured.

Figure 4 illustrates our flexible needle puncture mechanism considering insertion and rotation coupling. In this design, the RHILB is detachably mounted to the mechanism shell. The needle is secured to the lower needle holder. The RHILB is coaxially aligned with the needle axis, ensuring motion stability and accuracy of positioning. An extension arm integrated in the lower needle holder engages with the groove via sliding contact.

Moreover, the rotational DOFs of the upper needle holder are mechanically restricted by the cover plate. The force sensor is rigidly coupled to the upper needle holder, thereby eliminating rotational displacement of the sensor and effectively preventing cable entanglement issues. The force sensor is interfaced with the proximal end of the puncture needle, enabling the real-time quantification of the axial insertion forces.

Figure 5 illustrates the whole flowchart of the working principle. In our preconfigured LP procedure, the thickness of distinct tissue layers of the patient's lumbar region needs to be determined by undergoing an X-ray scan first, such as skin, adipose tissue, muscle, dura mater, etc. During the LP procedure, the needle punctures multiple layers of tissue. So, the RHILB was established which enables on-demand customization via 3D printing technology, customized to the patient-specific distribution of the tissue layers. The RHILB was then mounted to the mechanism shell.

When the motor drives the transmission gears to transmit power to the vertical inner sleeve, the vertical inner liner sleeve drives the rotation of the extension arm on the needle holder by means of its longitudinal slot. During this time, the extension arm slides along the spiral groove, inducing simultaneous rotational and linear motion of the puncture needle. Through this kinematic coupling, the IRR of the needle is accurately regulated by RHILB. The transition curve modulates IRR by altering the pitch of the screw.

4 Kinematic Modeling and Performance Analysis

4.1 Kinematic Modeling. When the proposed device driven by a single motor operates at the connection point between helices with different pitches, an abrupt change in pitch inevitably induces mechanical impacts, causing sudden variations in velocity and acceleration along the insertion direction. The variations severely affect the longevity of the mechanism and insertion

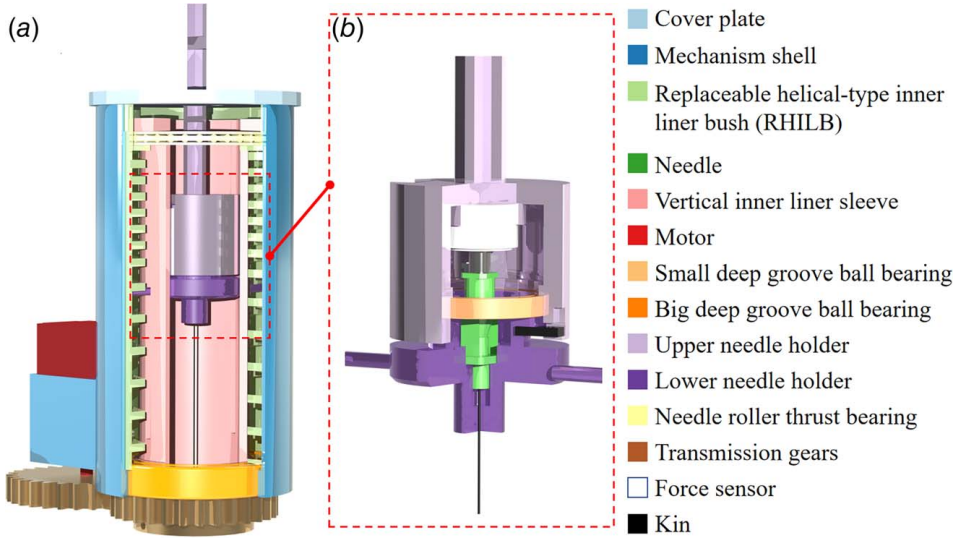

Fig. 4 Mechanical structure display: (*a*) Structure of the main transmission components and (*b*) the inner structure of the needle holder

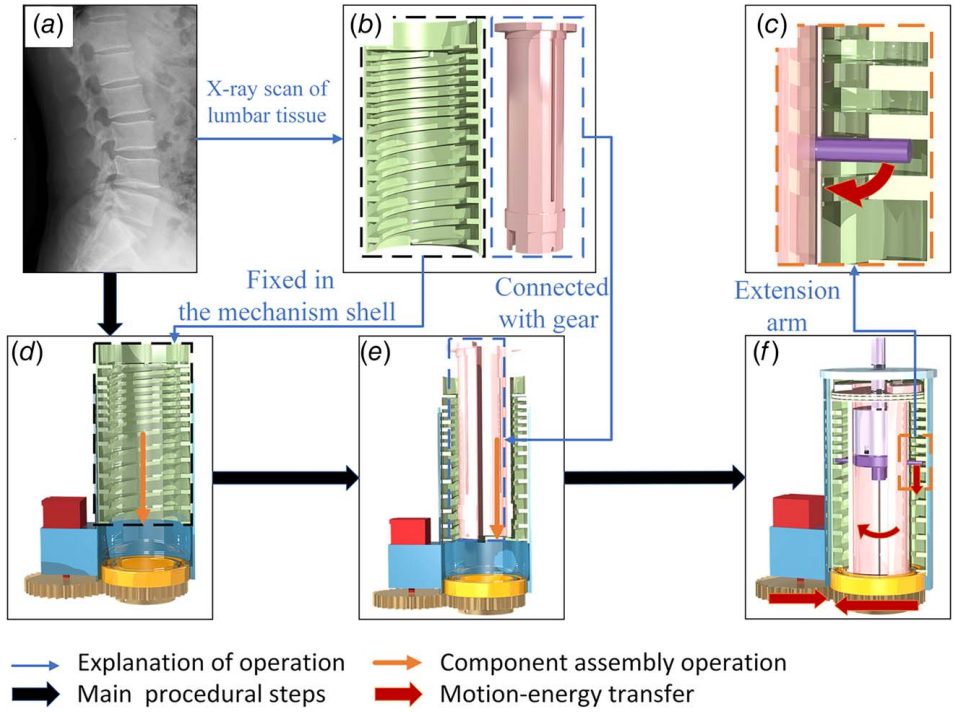

Fig. 5 Working principle display. (*a*) The image of distinct tissue layers of the patient's lumbar region obtained by X-ray. (*b*) The RHILB and the vertical inner liner sleeve were fabricated by 3D printing. (c) The assembly fit of the extension arm with RHILB and the vertical inner liner sleeve. (*d*) The combination of the RHILB and the mechanism shell. (e) The combination of the vertical inner liner sleeve and the RHILB. (*f*) The complete mechanism motion transmission process: the motor drives the vertical inner liner sleeve to generate rotational motion through the gear set, then the vertical inner liner sleeve transmits this rotational movement to the needle holder by carrying its extension arms, and the needle holder accomplishes a combined rotational and liner feed motion along the helical groove of the RHILB.

precision. A sudden pitch change would lead to an instantaneous change in needle insertion speed, thus causing needle vibration. The vibration would increase the shear force to the soft tissue, increasing the needle deflection and causing worse damage to tissues. Inside the mechanical structure, the abrasion of the screw fitting parts would be aggravated due to the instantaneous impact. We designed a model to smoothly connect the helices of different pitches by a fifth-order polynomial function curve. The core goal of the design is to eliminate mechanical impacts due to sudden acceleration changes, ensuring continuity of velocity and acceleration during punctures, thus improving device life and positioning accuracy. To avoid the problem, a transition helical curve is designed to smoothly connect helices of different pitches. The derivation of the transition curve is described as follows.

When the helical transmission mechanism is operated, there is a functional relationship between the depth of the feed and the angle of rotation along the helix. Therefore, we model the curve in the cylindrical coordinate system (R, ψ, Z):

- The positive direction of Z-axis is defined as the insertion feed direction;
- ψ is defined as the counterclockwise rotation angle around Z-axis (assuming helical direction is counterclockwise);
- R is defined as the radius of the helix projected onto the plane perpendicular to Z-axis.

The helical transition curve is expressed as a polynomial function:

$$Z = F(\psi) = a_0 + a_1\psi + a_2\psi^2 + a_3\psi^3 + \cdots + a_n\psi^n \tag{1}$$

where a_0 to a_n are coefficients determined by the boundary conditions mentioned in the next part.

The function of feed velocity along the Z-axis is

$$v(\psi) = \frac{dF}{dt} \tag{2}$$

$$\begin{aligned} &= a_1\frac{d\psi}{dt} + a_2 2\psi\frac{d\psi}{dt} + \cdots + a_n n\psi^{n-1}\frac{d\psi}{dt} \\ &= \frac{d\psi}{dt}\left(a_1 + 2a_2\psi + \cdots + na_n\psi^{n-1}\right) \end{aligned} \tag{3}$$

The mechanism is driven by a single motor with a fixed angular velocity of ω, namely $d\psi/dt = \omega$ is a constant.

The function of feed acceleration along the Z-axis is

$$a(\psi) = \frac{dv}{dt} \tag{4}$$

$$\begin{aligned} &= \frac{d\psi}{dt}\left(2a_2\frac{d\psi}{dt} + \cdots + n(n-1)a_n\psi^{n-2}\frac{d\psi}{dt}\right) \\ &= \omega^2\left(2a_2 + 6a_3\psi + \cdots + n(n-1)a_n\psi^{n-2}\right) \end{aligned} \tag{5}$$

In the case of insertion into two-layer tissue (tissue 1 and tissue 2) with different optimal IRRs, k_1 (mm/r) for tissue 1 and k_2 (mm/r) for tissue 2, the transition curve functions must satisfy the specific boundary conditions, which are expressed as the following equations:

$$\begin{cases} llF(0) = z_0 \\ v(0) = \omega a_1 = \frac{\omega k_1}{2\pi} \\ a(0) = \omega^2 2a_2 = 0 \\ F(\theta) = a_0 + a_1\theta + a_2\theta^2 + \cdots + a_n\theta^n = h + z_0 \\ v(\theta) = \omega\left(a_1 + 2a_2\theta + \cdots + na_n\theta^{n-1}\right) = \frac{\omega k_2}{2\pi} \\ a(\theta) = \omega^2\left(2a_2 + \cdots + n(n-1)a_n\theta^{n-2}\right) = 0 \end{cases}$$

where h is the height in the Z-axis direction of the transition curve and θ is the angle around the Z-axis of the transition curve, both previously given by the designer.

According to the boundary conditions, only the six equations below can be derived, so the nth-order polynomial of the transition curve is simplified to a fifth-order polynomial, and the higher order term is ignored:

$$\begin{cases} F(0) = z_0 & \text{initial position} \\ v(0) = \dfrac{\omega k_1}{2\pi} & \text{initial velocity} \\ a(0) = 0 & \text{initial acceleration} \\ F(\theta) = h + z_0 & \text{final position} \\ v(\theta) = \dfrac{\omega k_2}{2\pi} & \text{final velocity} \\ a(\theta) = 0 & \text{final acceleration} \end{cases}$$

The coefficients are solved as

$$\begin{cases} a_0 = z_0 \\ a_1 = \dfrac{k_1}{2\pi} \\ a_2 = \dfrac{10h}{\theta^3} + \dfrac{1}{\pi\theta^2}(-3k_1 - 2k_2) \\ a_4 = -\dfrac{15h}{\theta^4} + \dfrac{1}{\pi\theta^3}\left(4k_1 + \dfrac{7}{2}k_2\right) \\ a_5 = \dfrac{6h}{\theta^5} - \dfrac{1}{\pi\theta^4}\left(\dfrac{3}{2}k_1 + \dfrac{3}{2}k_2\right) \end{cases} \tag{6}$$

The final helical transition curve function is

$$\begin{aligned} F(\psi) = z_0 &+ \frac{k_1}{2\pi}\psi + \left[\frac{10h}{\theta^3} + \frac{1}{\pi\theta^2}(-3k_1 - 2k_2)\right]\psi^3 \\ &+ \left[-\frac{15h}{\theta^4} + \frac{1}{\pi\theta^3}\left(4k_1 + \frac{7}{2}k_2\right)\right]\psi^4 \\ &+ \left[\frac{6h}{\theta^5} - \frac{1}{\pi\theta^4}\left(\frac{3}{2}k_1 + \frac{3}{2}k_2\right)\right]\psi^5 \end{aligned} \tag{7}$$

The velocity and acceleration functions in the Z-axis direction are

$$\begin{aligned} v(\psi) = \frac{k_1}{2\pi}\omega &+ \left[\frac{10h}{\theta^3} + \frac{1}{\pi\theta^2}(-3k_1 - 2k_2)\right]3\psi^2\omega \\ &+ \left[-\frac{15h}{\theta^4} + \frac{1}{\pi\theta^3}\left(4k_1 + \frac{7}{2}k_2\right)\right]4\psi^3\omega \\ &+ \left[\frac{6h}{\theta^5} - \frac{1}{\pi\theta^4}\left(\frac{3}{2}k_1 + \frac{3}{2}k_2\right)\right]5\psi^4\omega \end{aligned} \tag{8}$$

and

$$\begin{aligned} a(\psi) = \omega^2\Bigg\{ &6\left[\frac{10h}{\theta^3} + \frac{1}{\pi\theta^2}(-3k_1 - 2k_2)\right]\psi \\ &+ 12\left[-\frac{15h}{\theta^4} + \frac{1}{\pi\theta^3}\left(4k_1 + \frac{7}{2}k_2\right)\right]\psi^2 \\ &+ 20\left[\frac{6h}{\theta^5} - \frac{1}{\pi\theta^4}\left(\frac{3}{2}k_1 + \frac{3}{2}k_2\right)\right]\psi^3\Bigg\} \end{aligned} \tag{9}$$

Thus, the kinematic equations for the transition helical curve have been established in the cylindrical coordinate system.

4.2 Performance Analysis. Based on the parameters obtained in Secs. 2 and 3, we precisely calculate the fifth-order polynomial of the transition curve using the aforementioned equations. Thus, the specific shape of the helical part of the RHILB was determined and subsequently applied in the experiments described in Sec. 5. The specific parameters can be found in Table 1.

The value of h has a significant influence on the transition performance of the feed velocity and acceleration in the Z-axis direction. We analyzed the performance of the curves with different h and the results are shown in Fig. 6, demonstrating the best performance corresponding to $h = 5$ mm.

Table 1 Parameters determined by experimental conditions

Number	Parameter	Description
1	$k_1 = 12$ mm	Pitch 1
2	$k_2 = 26$ mm	Pitch 2
3	$\omega = 0.4\,\pi$ rad s^{-1}	Angular velocity
4	$\theta = 0.5\,\pi$ rad	Transition angle
5	$z_0 = 0$ mm	Initial Z-axis position
6	$R = 34$ mm	Helix radius
7	$h = 5$ mm	Z-axis length of curve

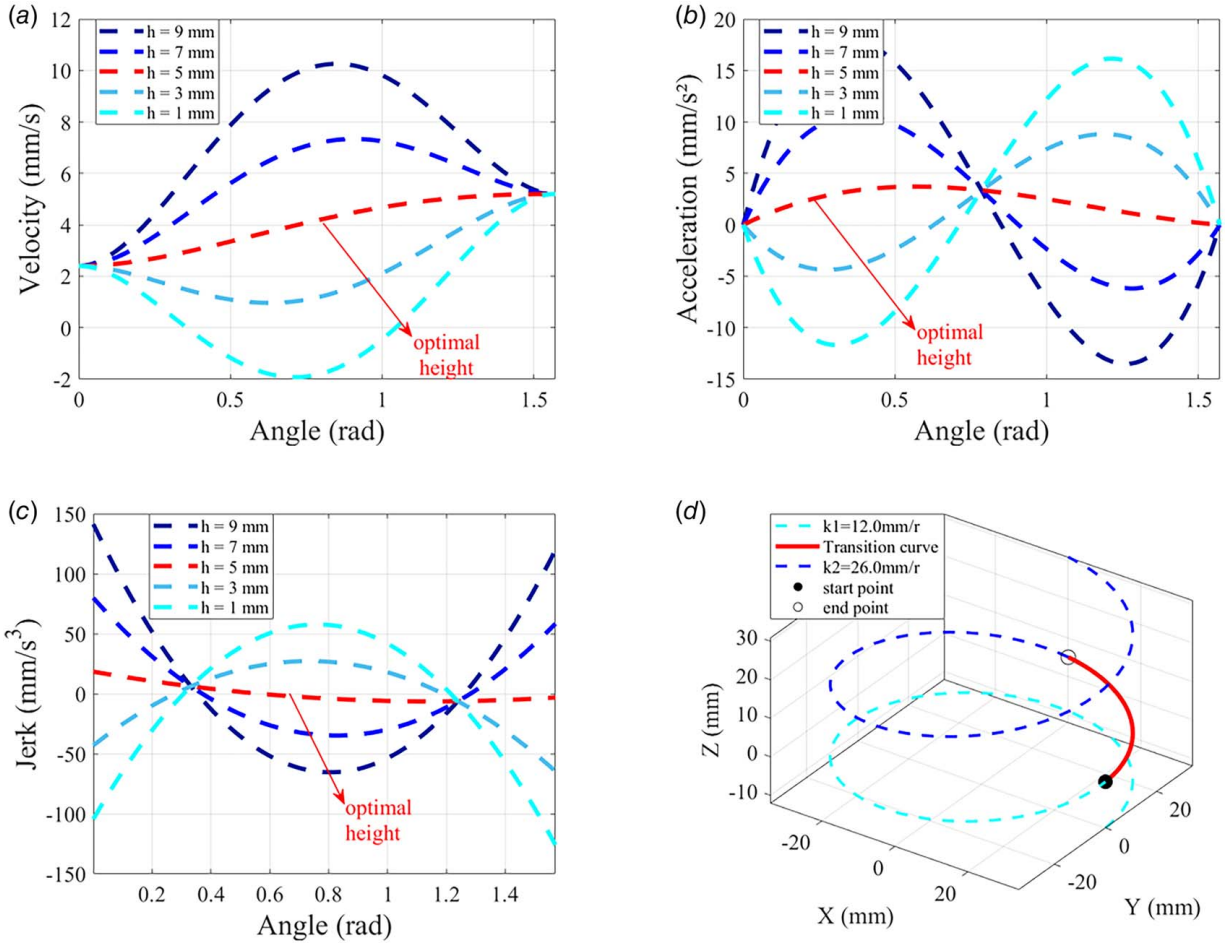

Fig. 6 The figure illustrates the curves (when *h* differs) of the insertion velocity, acceleration, and jerk along the *Z*-axis as the angle of rotation changes when the mechanism runs along the transition curve at a constant angular velocity. (*a*) Transition velocity curves. (*b*) Transition acceleration curves. (*c*) Transition jerk curves. (*d*) The illustration of the helical transition curve. When $h = 5$ mm, the velocity curve fluctuates the least, demonstrating that it can implement the smoothest velocity transition between the velocities determined by two helices. Also, the acceleration has minimal fluctuations and is always non-negative. It demonstrates that under this condition, the movement process is most stable, and the velocity increases monotonically. The jerk curve corresponding to $h = 5$ mm presents the smoothest trend with only one zero, indicating that the average slope and peak value of the acceleration curve are both minimum. The modeled helical transition curve with a height of 5 mm smoothly connecting the helices with pitches of 12 mm/r and 26 mm/r is drawn in a coordinate system.

5 Experimental Evaluation

The present study was designed to achieve two primary objectives: to investigate the impact of RHILB on accuracy and to show that the actual motion curve of the needle strongly correlates with the theoretical curve.

5.1 Experimental Setup. Based on the characteristic differences between material A and material B (12 mm/r for material A and 26 mm/r for material B), three types of RHILBs were designed and fabricated: RHILB I featured a variable-pitch configuration with a transition curve, where the upper section ($L = 30$ mm) adopted a spiral structure with a pitch value of 12 mm/r, while the lower section ($L = 25$ mm) was adjusted to a pitch of 26 mm/r; RHILB II was a uniform-pitch structure ($P = 12$ mm/r); and RHILB III was a uniform-pitch structure ($P = 26$ mm/r). All RHILBs were fabricated using stereolithography additive manufacturing technology with Futura 8200Pro resin, achieving dimensional accuracy within ± 0.1 mm.

To systematically investigate the synergistic effects of material properties and spiral structure, three targeted material configurations were established: group I comprised a composite layered structure (total thickness: 6 cm) with a 3 cm surface layer of material A and a 3 cm base layer of material B; group II was a homogeneous structure of material A (thickness is 6 cm); and group III was a homogeneous structure of material B (thickness is 6 cm). A full factorial experimental design was implemented, resulting in nine test conditions (3 RHILBs × 3 target material configurations). Each condition was repeated for eight valid puncture distances to ensure statistical significance.

The puncture testing platform comprised the proposed RNID, a force sensor (SBT674, SIMBATOUCH Co., Ltd, Guangzhou, China), and a digital oscilloscope (RIGOL DS1104, RIGOL TECHNOLOGIES Co., Ltd, Beijing, China). The puncture needle (disposable nerve blocking needle, Jiangsu Huaxing Medical Equipment Industry Co., Ltd, Yangzhou, China) was accurately controlled by a motor driver (DM420, Yixuan Yun Kong Technology Co., Ltd, Beijing, China) and pulse transmitter (CL-01A single-axis intelligent controller, Beijing Haijiejiachuang Techology Co., Ltd, Beijing, China). The needle maintained a constant angular velocity of 12 rpm (period: 5 s/r). The deflection of the needle tip was quantified using the methodology described in Sec. 2.

The dynamic displacement of the needle was guided by the transition curve and characterized using a laser displacement sensor (HG-C1030, Panasonic, Ltd, Japan). As shown in Fig. 7, the checking point was set in the upper needle holder, because it was rigidly

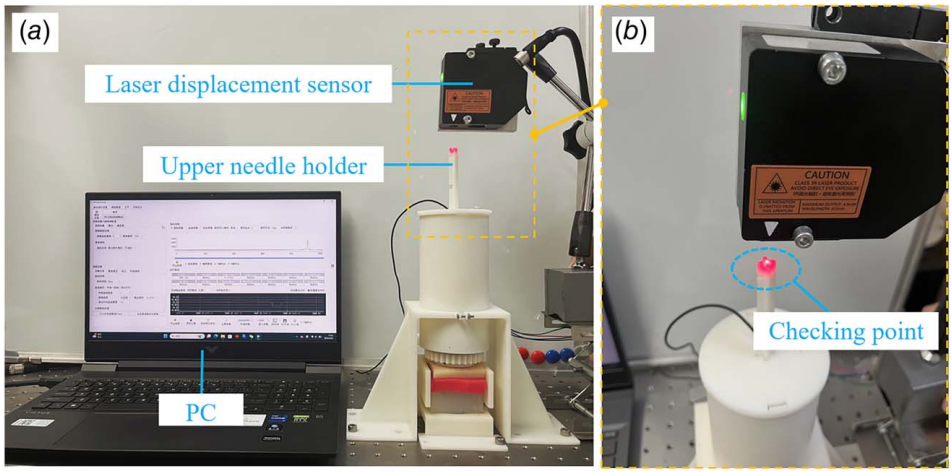

Fig. 7 The dynamic displacement of the needle through the transition curve is captured by laser rangefinder: (*a*) setting of the displacement capture experimental platform and (*b*) a close-up of the checking point

connected with the needle in the vertical direction. The motion trajectory data of the needle were acquired to systematically analyze variations in kinematic parameters (velocity and acceleration). To increase the visual effect, the constant angular velocity was set to 24 rpm (period: 2.5 s/r) and the sampling interval of 80 μs was applied.

5.2 Results and Analysis

5.2.1 Effects of Deflection. During the experiment, we found that if we collected eight distances (nine puncture points) with one test paper, it would cause the puncture points to overlap, which was not conducive to further measurement. So the team decided to adopt a 5 + 3 data collection method, that is, using two test papers to measure 5 and 3 data points, respectively. Figure 8 shows the test papers of five data. The comparative analysis of the needle tip deflection distribution is shown in Fig. 9(*a*), and quantitative statistical results are shown in Table 2. The results revealed that the bush with variable-pitch configuration (RHILB I) demonstrated superior trajectory control performance during the multilayer composite puncture. The average needle tip deflection for RHILB I was 0.933 mm, representing a reduction of 27.73% ($p < 0.05$) compared to the uniform-pitch structure (RHILB II, $P = 12$; 1.291 mm) and a 62.4% decrease ($p < 0.001$) relative to the uniform-pitch structure (RHILB III, $P = 26$; 2.476 mm). This phenomenon can be attributed to the variable-pitch configuration, which effectively accommodates the IRR differences between material A and material B, and effectively reduces the deflection caused by the oblique force on the needle in different materials.

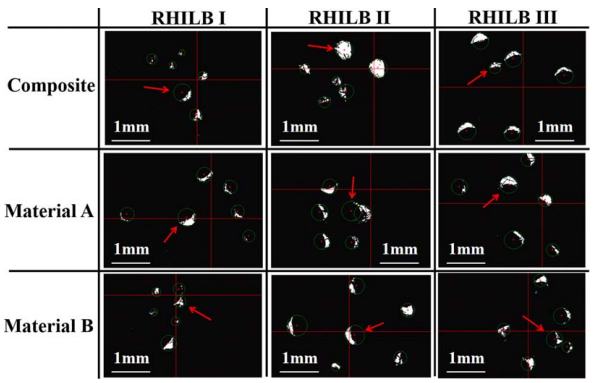

Fig. 8 Observation results of optical measuring instruments in different groups. The arrows point to the empty puncture point (the theoretical target point), and the others are material-filled puncture points. The line segments represent the scale. The circles are the pinhole fitting circles.

In puncture tests with homogeneous material A, RHILB II ($P = 12$ mm/r) demonstrated optimal trajectory stability, with an average deflection of 0.734 mm. Interestingly, in experiments using homogeneous material B, although theoretical models predicted that RHILB III ($P = 26$ mm/r) should exhibit optimal compatibility, experimental data revealed that RHILB I achieved a lower deflection (1.265 mm), representing a 4.38% reduction compared to RHILB III (1.323 mm). Further analysis of the IRR curve of material B revealed that the deflection differences were relatively small at $P = 12$ mm/r and $P = 26$ mm/r, which may originate from the nonlinear variation characteristics of the IRR curve. Material B exhibited substantially higher viscoelasticity than material A. This intrinsic property amplified minor experimental variations into significant IRR deviations during repetitive testing. This has led to its manifestation of nonlinear characteristics.

This study systematically validated the nonlinear coupling mechanisms between spiral parameters and material properties through full-factorial experimental investigations. The results demonstrated that the variable-pitch bush (RHILB I) achieves an improvement of 27.73–62.40% in multimaterial puncture accuracy.

5.2.2 Effects of Needle Kinematics. Experimental results were collected through a dynamic capture system of the features of the needle, resulting in a valid sample size of $N = 8667$. A fifth-order polynomial regression model was utilized to fit the displacement–angle relationship, achieving a coefficient of determination (R^2) of 0.993 and a root mean square error (RMSE) of 0.0723. As illustrated in Fig. 9(*b*), the fitted curve exhibited significant consistency with the theoretical model derived in Sec. 4 during the primary motion phases (Pearson correlation coefficient $r = 0.9991$).

Subsequently, the kinematic parameters were calculated using numerical differentiation: first- and second-order derivatives of the displacement–angle function $s(\psi)$ yielded velocity $v(\psi)$ and acceleration $a(\psi)$ (Figs. 9(*c*) and 9(*d*)). Quantitative analysis revealed a near-perfect alignment between the experimental and theoretical velocity curves (Pearson correlation coefficient $r = 0.99970$), while the acceleration profiles showed strong correlation ($r = 0.99691$). These results indicate that the deflection between the observed needle kinematics and the theoretical design parameters remain within engineering tolerance thresholds, validating the reliability of the proposed dynamic model.

6 Discussions

This article proposes a patient-specific RNID with 1-DOF. The 1-DOF motion is coupled with both insertion and rotation to

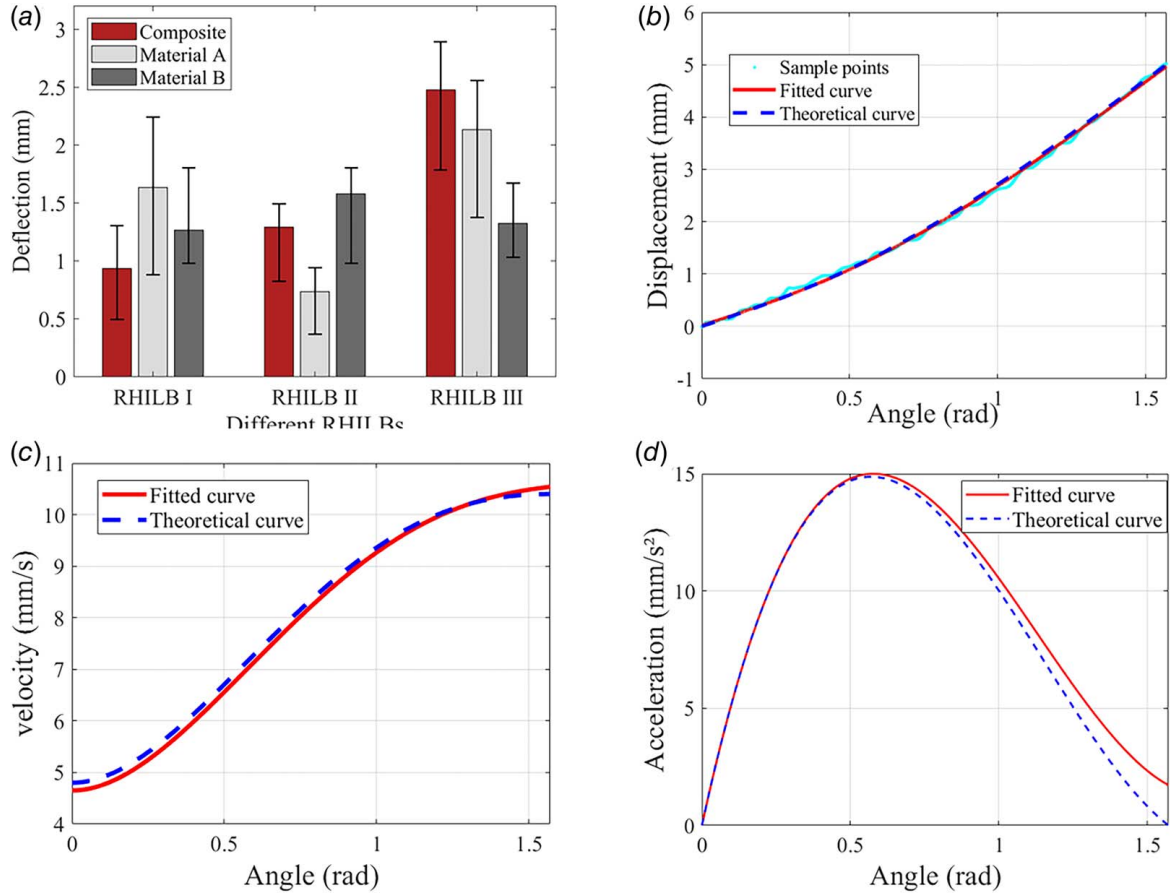

Fig. 9 Results of the proposed RNID. (*a*) Comparison of the needle tip deflection between different RHILBs and different materials. The top of the bar chart represents the average deflection, and the error bar represents the maximum and minimum values in each sample group. (*b*) The results of collecting and fitting the dynamic displacement of the needle. Comparison diagram of the fitted displacement curve and the theoretical displacement curve. (c) Comparison diagram of the fitted velocity curve and the theoretical velocity curve. (*d*) Comparison diagram of the fitted acceleration curve and the theoretical acceleration curve.

Table 2 Statistics for tip deflection quantification

	Deflection (mm)		
	RHILB I	RHILB II	RHILB III
Composite	0.933	1.291	2.476
Material A	1.634	0.734	2.132
Material B	1.265	1.578	1.323

reduce the needle deflection. A RHILB can achieve dynamic adaptation for the mechanical properties of the multilayered tissues. Introducing a transition curve model to facilitate the smooth connection of spiral modules with varying pitches. The curve ensures speed continuity and no mechanical impact.

6.1 Clinical Adaptability. In this article, the RNID adopts an RHILB, and a customized puncture system can be generated according to the patient's condition by combining with 3D printing technology. This is applicable to not only the vast majority of patients but also greatly reduces the additional costs caused by the mismatch between the puncture system and the patients. Then, the puncture system is driven by a single motor. Compared with the multimotor coupling drive of other puncture systems, it has the advantages of a smaller size and simpler operation.

6.2 Mechanical Analysis of Insertion-Rotation Ratio. When the IRR is too small, the fine flexible needle experiences a reaction force perpendicular to its bevel during insertion. Due to slow rotation, cumulative microdeflections are induced by this force concentrated in one direction, causing bending deformation of the needle. When the IRR is too large, significant circumferential deformation occurs in the flexible needle due to excessive friction torque from the surrounding tissue. This results in substantial misalignment between the needle tip and the needle hub, leading to large errors. Consequently, for a given material and our fine flexible needle, there must exist an optimal IRR between excessively small and large values.

6.3 Limitations

6.3.1 Error in Repeated Insertions. Due to tissue heterogeneity, repeated insertions lead to relatively large errors, resulting in imprecise experimental results of the optimal IRR. Although experiments have verified that using the optimal IRR can reduce errors, exceptional cases still exist. As shown in Table 2, although theoretical models predicted that RHILB III ($P = 26$ mm/r) should exhibit optimal compatibility, experimental data revealed that RHILB I achieved a lower deflection (1.265 mm), representing a 4.38% reduction compared to RHILB III (1.323 mm).

6.3.2 Material Limitation. Although we have verified that different tissues have optimal IRRs for minimal deflection, all experiments were carried out in silicone simulation models. New challenges may arise when translating these findings into human tissues, where optimal IRRs remain unknown.

6.4 Challenges. Human tissues such as skin, fat, and ligaments show nonlinear viscoelastic, anisotropic, and unique dynamic characteristics, which could not be provided by silicone materials used in our experiments. This would lead to the possibility that the best IRR obtained from the static model may not be applicable to live tissue. In addition, the geometry data provided by CT/X-ray before the procedure cannot quantify the real-time mechanical properties, and the real-time force feedback signal may need to be integrated with AI in the future to dynamically adjust the needle insertion process. What is more, patient-specific RHILB 3D printing adds preoperative time (minutes–hours), which is impractical for emergency procedures. Custom RHILB per patient may be prohibitively expensive compared to conventional needles, limiting adoption.

7 Conclusions

Robotic-assisted LP has been explored in recent years, and spiral drive-based RNID has received considerable critical attention. Exploring the optimal IRRs for different materials can assist in designing the corresponding spiral of the pitch and inserting it to achieve the minimum deflection of the needle tip. In this work, we have verified that RNID based on variable IRRs leads to a smaller deflection than the ones with constant IRR in a two-layer phantom. Furthermore, the kinematic model of the spiral transition curve is derived to avoid sharp changes in speed or acceleration during insertion.

In our future work, there are several directions that we need to continue to study in depth. First, it is necessary to determine whether rotation will aggravate the problems of surgical trauma and pain, and formulate relief strategies. Second, conduct mechanical modeling of the material and give a reasonable explanation for the nonlinear characteristics of material B.

Acknowledgment

This work is supported by Undergraduate Education and Teaching Reform Research Project of Nanjing University of Aeronautics and Astronautics (Grant No. 2023JG0524Y) and International Joint Laboratory of Sustainable Manufacturing, Ministry of Education and the Fundamental Research Funds for the Central Universities (Grant No. NG2024016).

Conflict of Interest

There are no conflicts of interest.

Data Availability Statement

The authors attest that all data for this study are included in the article.

Nomenclature

Abbreviations

3D	=	three-dimensional
CT	=	computed tomography
DOF	=	degree-of-freedom
IRR	=	insertion-rotation ratio
LP	=	lumbar puncture
RNID	=	robotic-assisted needle insertion device
RHILB	=	replaceable helical-type inner liner bush
RMSE	=	root mean square error

References

[1] Patel, B. R., Maire, A., Frances, S., Joanna, F., and Matthew, K., 2022, "Retrospective Study Comparing Success Rates of Lumbar Puncture Positions in Infants," Am. J. Emerg. Med., **56**, pp. 228–231.

[2] Li, Y., and Li, H., 2024, "Penetration Event Identification Based on Neural Network for Needle Tip Location in Robot Assisted Lumbar Puncture Surgery," IEEE Robot. Autom. Lett., **9**(1), pp. 343–350.

[3] Bedetti, L., Lugli, L., Marrozzini, L., Alessandro, B., Leone, F., Baroni, L., and Laura, L., 2021, "Safety and Success of Lumbar Puncture in Young Infants: A Prospective Observational Study," Front. Pediatr., **9**, p. 692652.

[4] Siddharth, N., Alex, K., Jaeschke, R., Sharma, S., Laura, B., Shoamanesh, A., and Singh, S., 2018, "Atraumatic Versus Conventional Lumbar Puncture Needles: A Systematic Review and Meta-analysis," Lancet, **391**(10126), pp. 1197–1204.

[5] Wang, J., Miao, J., Yi, Z., Duan, Y., Wang, Y., Hao, D., and Wang, B., 2023, "Spine Surgical Robotics: Current Status and Recent Clinical Applications," Neuropsine, **20**(4), pp. 1256–1271.

[6] Yu, Z., Duan, Y., Zhang, L., and Ling, J., 2024, "A Patient-Mounted Spherical Scissor-Like Remote Center of Motion Mechanism for Robotic-Assisted Lumbar Puncture," International Conference on Intelligent Robotics and Applications, Xi'an, China, July 31–Aug. 2, pp. 115–129.

[7] Duan, Y., Ling, J., Feng, Z., Yao, D., and Zhu, Y., 2024, "Development of a Base-Actuated Three-Rhombus Configured Remote Center of Motion Mechanism for Lumbar Puncture," ASME J. Mech. Rob., **16**(5), p. 054503.

[8] Duan, Y., Ling, J., Feng, Z., Ye, T., Sun, T., and Zhu, Y., 2024, "A Survey of Needle Steering Approaches in Minimally Invasive Surgery," Ann. Biomed. Eng., **52**(6), pp. 1492–1517.

[9] Wang, C., Li, G., Zhu, J., Zhu, L., Li, C., Zhu, H., Song, A., et al., 2024, "Review of Robotic Systems for Thoracoabdominal Puncture Interventional Surgery," APL Bioeng., **8**(2), p. 021501.

[10] Ehrampoosh, A., Shirinzadeh, B., Pinskier, J., Smith, J., Moshinsky, R., and Zhong, Y., 2022, "A Force-Sensing Semi-automated Robotic Needle Driver for Minimally Invasive Surgery," 25th International Conference on Mechatronics Technology (ICMT 2022), Kaohsiung, Taiwan, China, Nov. 18–21, pp. 1–5.

[11] Lu, J., Huang, Z., Zhuang, B., Cheng, Z., Jing, G., and Lou, H., 2023, "Development and Evaluation of a Robotic System for Lumbar Puncture and Epidural Steroid Injection.," Front. Neurorobot., **17**, p. 1253761.

[12] Xuan, X., Chen, L., Hu, X., Wang, Y., Saini, A., Liu, T., Yang, K., Zhu, Y., and Jin, H., 2024, "Ultrasound Robotic System to Multi-approach Puncture for Endoscopic Spinal Surgery," IEEE Robot. Autom. Lett., **9**(10), pp. 9119–9126.

[13] Trączyński, M., Patalas, A., Rosłan, K., Suszyński, M., and Talar, R., 2024, "Assessment of Needle–Tissue Force Models Based on Ex Vivo Measurements," J. Mech. Behav. Biomed. Mater., **150**, p. 106247.

[14] Wang, Y., Kwok, K. W., Kevin, C., Taylor, R. H., and Iulian, I., 2023, "Flexible Needle Bending Model for Spinal Injection Procedures," IEEE Robot. Autom. Lett., **8**(3), pp. 1343–1350.

[15] Lei, Y., Du, S., Li, M., Tian, X., Hu, Y., and Wang, Z., 2024, "Needle-Tissue Interaction Model Based Needle Path Planning Method.," Comput. Methods Prog. Biomed., **243**, p. 107858.

[16] Li, H., Xun, N., Ding, D., Li, Y., Zhang, J., Min, Z., and Evgeni, M., 2022, "An Admittance-Controlled Amplified Force Tracking Scheme for Collaborative Lumbar Puncture Surgical Robot System," Int. J. Med. Robot. Comput. Assist Surg., **18**(5), p. e2428.

[17] Ogawa, T., Saito, R., and Iwata, H., 2022, "Novel Transmission Mechanism (Shaft-Following Gear Mechanism) Applied to a Puncture Robot for Three Dimensional Punctures," 2022 International Symposium on Measurement and Control in Robotics (ISMCR), Houston, TX, Sept. 28–30, pp. 1–4.

[18] Zhao, Y., Zhang, H., Hai, Y., Qian, C., Jin, Y., Chen, Y., and Yang, G., 2025, "Path Planning for Flexible Needle Based on Both Insertion Mechanism Kinematics and Needle Bending Model," Phys. Med. Biol., **70**(1), p. 015016.

[19] Wang, R., Tan, G., and Liu, X., 2023, "Robust Tip Localization Under Continuous Spatial and Temporal Constraints During 2D Ultrasound-Guided Needle Puncture.," Int. J. Comput. Assist. Radiol. Surg., **18**(12), pp. 2233–2242.

[20] Scali, M., Breedveld, P., and Dodou, D., 2019, "Experimental Evaluation of a Self-Propelling Bio-Inspired Needle in Single- and Multi-layered Phantoms," Sci. Rep., **9**, p. 19988.

[21] Leibinger, A., Oldfield, M. J., and Rodriguez y Baena, F., 2016, "Minimally Disruptive Needle Insertion: A Biologically Inspired Solution," Interface Focus, **6**(3), p. 20150107.

[22] Bloemberg, J., Trauzettel, F., Coolen, B., Dodou, D., and Breedveld, P., 2022, "Design and Evaluation of an MRI-Ready, Self-propelled Needle for Prostate Interventions," PLoS One, **17**(9), p. e0274063.

[23] Badaan, S., Doru, P., Kim, C., Pierre, M., Mazilu, D., Gruionu, L., Patriciu, A., Kevin, C., and Stoianovici, D., 2011, "Does Needle Rotation Improve Lesion Targeting?" Int. J. Med. Robot. Comput. Assist. Surg., **7**(2), pp. 138–147.

[24] Stoianovici, D., Kim, C., Petrisor, D., Jun, C., Lim, S., Ball, M. W., Ross, A., Macura, K. J., and Allaf, M. E., 2017, "MR Safe Robot, FDA Clearance, Safety and Feasibility of Prostate Biopsy Clinical Trial," IEEE/ASME Trans. Mechatron., **22**(1), pp. 115–126.

[25] Zemiti, N., Morel, G., Tobias, O., and Nicolas, B., 2007, "Mechatronic Design of a New Robot for Force Control in Minimally Invasive Surgery," IEEE/ASME Trans. Mechatron., **12**(2), pp. 143–153.

[26] Swensen, J. P., Mingde, L., Okamura, A. M., and Cowan, N. J., 2014, "Torsional Dynamics of Steerable Needles: Modeling and Fluoroscopic Guidance," IEEE Trans. Biomed. Eng., **61**(11), pp. 2707–2717.

[27] Engh, J. A., Minhas, D. S., Kondziolka, D., and Riviere, C. N., 2010, "Percutaneous Intracerebral Navigation by Duty-Cycled Spinning of Flexible Bevel-Tipped Needles," Neurosurgery, **67**(4), pp. 1117–1123.